Bio-Design and Manufacturing (2025) 8:1009–1023
https://doi.org/10.1631/bdm.2500004

RESEARCH ARTICLE

Miniature Ni-diamond wheel for drilling and grinding of calcified plaque surrogate in chronic total occlusion treatment

Zhaokun Zhang[1] · **Jessie Jingxuan Lyu**[1] · **Yihao Zheng**[2] · **Hitinder S. Gurm**[3] · **Albert J. Shih**[1,4]

Received: 3 January 2025 / Accepted: 17 June 2025 / Published online: 5 November 2025

Abstract

Chronic total occlusion (CTO) is a cardiovascular disease in which coronary arteries are completely obstructed by atherosclerotic plaques for more than three months. Percutaneous coronary intervention (PCI) treatment of calcified CTO is challenging because hardened plaques prevent the crossing and delivery of microcatheters and balloons. In this study, a two-step atherectomy method for CTO treatment using a miniature electroplated nickel (Ni)-diamond wheel is proposed. The Ni-diamond wheel first drills a hole in the CTO lesion with rotational and oscillatory translational motion along a guidewire and then grinds the lesion using orbital motion to enlarge the hole beyond the diameter of the grinding wheel. The feasibility of the proposed two-step atherectomy method, combining drilling and grinding, and the forces exerted during drilling and grinding were experimentally investigated using two types of calcified CTO plaque surrogates: gypsum cement and ex vivo bovine bone. Drilling experiments were conducted in both manual and automated feeding modes. The experimental results demonstrate that the proposed miniature wheel drills through both types of CTO surrogates in the manual and automated feeding modes with more consistent drilling forces of approximately 0.046 and 0.027 N in the rapid and slow modes under automated feeding, respectively, than under manual feeding. During grinding, the miniature wheel generates orbital motion in the hole and expands the hole diameter from 0.85 to 1.26 mm within 120 s. The proposed integrated drilling and grinding approach has promise in addressing the clinical challenges of microcatheter- and balloon-uncrossable lesions in PCI treatment of CTO.

Graphical abstract

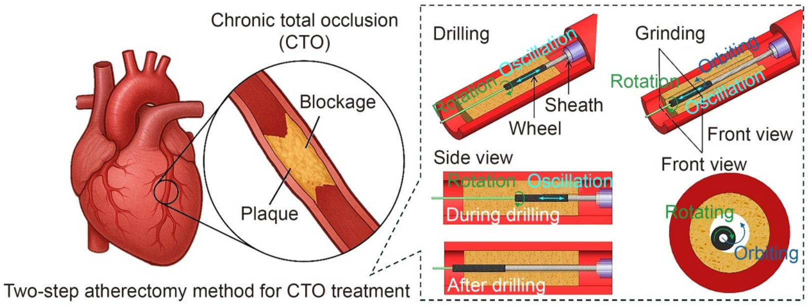

Keywords Chronic total occlusion · Miniature wheel · Drilling · Grinding · Force · Orbital motion

---

Zhaokun Zhang and Jessie Jingxuan Lyu have contributed equally to this work.

✉ Zhaokun Zhang
zhaokunz@umich.edu

[1] Department of Mechanical Engineering, University of Michigan, Ann Arbor, MI 48109, USA

[2] Department of Mechanical and Materials Engineering, Worcester Polytechnic Institute, Worcester, MA 01609, USA

[3] Division of Cardiovascular Medicine, Department of Internal Medicine, University of Michigan, Ann Arbor, MI 48109, USA

[4] Department of Biomedical Engineering, University of Michigan, Ann Arbor, MI 48109, USA

1 Introduction

Chronic total occlusion (CTO) is the total obstruction of a coronary artery by atherosclerotic plaque for a duration longer than three months with no perfusion, and it corresponds to zero in the thrombolysis in myocardial infarction risk score [1]. As shown in Fig. 1, CTO usually occurs in the proximal to middle locations of the right coronary artery, left circumflex artery, and left anterior descending artery among coronary arteries. CTO can lead to acute coronary syndrome (angina, shortness of breath, fatigue, etc.) [2] and an increased risk of mortality [3]. CTO is common in patients with coronary artery disease (CAD). In the U.S., there are more than 16.3 million patients with CAD [4], and the prevalence of patients with CTO varies in different studies, ranging from 29% to 52% [1, 5, 6]. Outside the U.S., the prevalence rates of patients with CTO are 33% in Germany [6], 12%–21% in the Netherlands [7], and 18% in Canada [8].

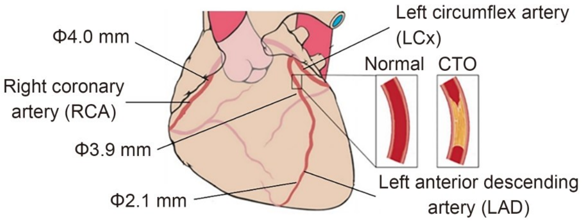

Fig. 1 Schematic of three common locations of CTO

Percutaneous coronary intervention (PCI) has been explored for minimally invasive treatment of CTO since the 1980s [9]. PCI uses a catheter (a thin flexible tube) with an inflatable balloon (for the angioplasty procedure) or a high-speed diamond wheel (for the atherectomy procedure) to open the narrowed vessel for deploying a stent and restoring blood flow. Typical catheterization procedures for PCI treatment of CTO (CTO-PCI) include the following six steps (Fig. 2a): Step 1 delivers a guide catheter near the proximal end of the CTO lesion; Step 2 inserts a CTO guidewire through the guide catheter and crosses the lesion; Step 3 inserts a microcatheter following the CTO guidewire; Step 4 removes the CTO guidewire from the microcatheter and leaves the microcatheter through the lesion; Step 5 inserts a PCI guidewire through the microcatheter; Step 6 removes the microcatheter and leaves the PCI guidewire in the lesion. Angioplasty (Fig. 2b) or atherectomy (Fig. 2c) may be performed after passing the PCI guidewire through the lesion [10, 11]. A successful CTO-PCI treatment procedure results in improved clinical outcomes, such as reduced angina symptoms, enhanced left ventricular systolic function, and decreased risk of arrhythmias, compared with conventional treatments, such as coronary artery bypass graft surgery [12–16].

CTO treatment with PCI is challenging. The current CTO-PCI success rate (55%–91%) [11, 17–19] is low compared with the regular PCI success rate (96%–99%) [20–22].

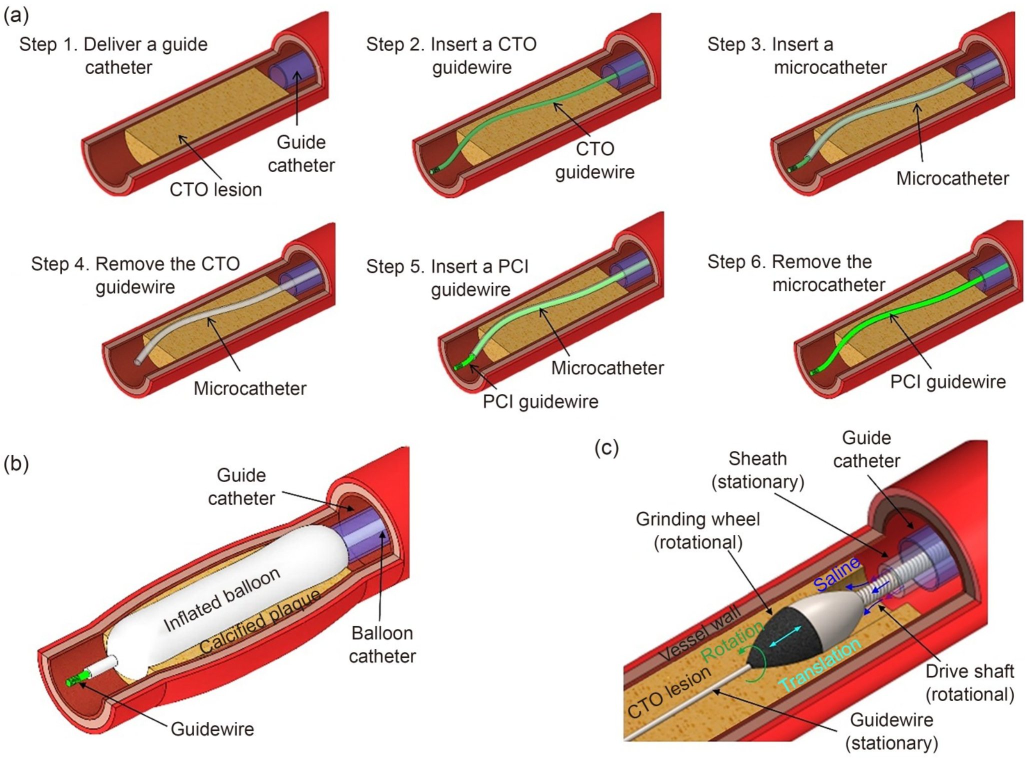

Fig. 2 Schematic of typical CTO-PCI catheterization procedure (a), balloon delivery and inflation in angioplasty (b), and atherectomy device for CTO treatment (c)

The following five conditions make the CTO-PCI procedure difficult: (1) blunt occlusion with no indication of the lumen, (2) calcification of the lesion, (3) tortuous lesions with a bending angle larger than 45°, (4) lesions longer than 20 mm, and (5) lesions previously attempted but failed [23]. Among these five conditions, severe lesion calcification is a strong predictor of CTO-PCI failure [24]. When severe lesion calcification occurs, key catheterization procedures (Step 3 in Fig. 2a) cannot be initialized because of resistance from the hardened calcified lesion [25]. In particular, a guidewire crossing (Step 2 in Fig. 2a) failure rate of 31.2% has been reported [11]. Clinicians are exploring clinical strategies, including improving guidewire control and selection [26, 27], dissection and re-entry techniques [28], retrograde approaches [29], and lesion modification techniques [30], for solving the wire-uncrossable problem. Even if the guidewire successfully crosses the CTO lesion, microcatheter and balloon insertion failures still occur, resulting in CTO-PCI failure. Previous studies have reported microcatheter insertion (Step 3 in Fig. 2a) failure rates of 11%–29% [25, 31, 32] and balloon delivery (Fig. 2b) failure rates of 10%–12% [33, 34]. These challenges highlight the need for a microcatheter device capable of crossing severely calcified and totally occluded lesions to handle microcatheter- and balloon-uncrossable lesions. Several techniques have been clinically adopted to tackle these challenges, including advanced catheters [35], balloon-assisted microdissection (BAM) [36], excimer laser coronary atherectomy (ELCA) [37], and rotational atherectomy (RA) [38]. Advanced catheters are designed to enhance catheter support or to provide specialized functionalities, such as screwability, to facilitate passage through the lesion [35]. BAM uses a small, low-profile balloon inserted into the lesion and inflated to rupture, creating microdissections that weaken the lesion [36]. ELCA uses ultraviolet light to treat plaque via photochemical ablation [37]. RA (Fig. 2c) uses a grinding wheel with abrasive grains to grind the lesion, thereby removing it and creating a lumen [38].

The aforementioned technologies for handling microcatheter- and balloon-uncrossable lesions have notable limitations. Advanced catheters, such as BAM and ELCA, are generally effective only for lesions with low calcification and struggle with highly calcified, high-hardness lesions. In addition, there is a risk of vessel perforation or dissection in BAM and ELCA. Although RA is capable of penetrating high-hardness lesions, it is associated with a high complication rate due to the large burr size and the high cutting force. A common challenge associated with these technologies is their difficulty in entering small arteries. The catheter or tool size for these methods typically ranges from 1.2 to 2.5 mm [39–41]. Given that the tool-to-artery diameter ratio is generally required to be less than 0.6, these devices are unsuitable for distal cardiovascular arteries with diameters of approximately 2 mm. This highlights the need for innovative technology capable of addressing uncrossable CTO lesions, particularly in narrow arteries.

To solve the problems of microcatheter- and balloon-uncrossable lesions in CTO-PCI, a new atherectomy approach using drilling and grinding with a miniature electroplated nickel (Ni)-diamond wheel is proposed in this study. Experiments of drilling and grinding of the calcified CTO lesion using the proposed approach are conducted using a cardiovascular simulation platform. The qualitative and quantitative investigations of the drilling and grinding forces on calcified CTO lesions provide insights into the combination of the drilling and grinding processes and evaluate the procedural feasibility for crossing and creating a lumen in the calcified CTO lesion for subsequent procedures.

2 Materials and methods

This section introduces the concept of the proposed two-step atherectomy method for CTO-PCI lesions using a miniature Ni-diamond wheel with sequential drilling and grinding, and the design of experiments for the verification of the proposed method based on a cardiovascular simulation platform.

2.1 Drilling and grinding of CTO lesions using a miniature Ni-diamond wheel

To handle microcatheter- and balloon-uncrossable lesions in CTO-PCI, a miniature Ni-diamond wheel with a sub-mm diameter was used to open the calcified CTO plaque. The procedure is depicted in Fig. 3, which includes four steps:

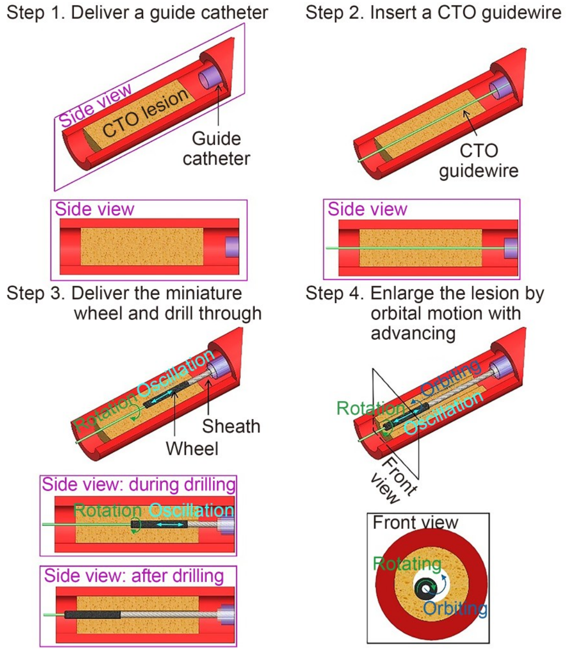

Fig. 3 Schematic of the CTO-PCI catheterization procedure using a miniature diamond wheel

Step 1 delivers a guide catheter near the proximal end of the CTO lesion, Step 2 inserts a CTO guidewire through the guide catheter and crosses the lesion, Step 3 delivers the miniature wheel with oscillatory translational–rotational motion along the guidewire to drill a hole in the calcified CTO plaque, and Step 4 enlarges the lumen by grinding with orbital motion inside the drilled hole. A millimeter-scale hole can be generated for subsequent PCI procedures. The proposed atherectomy approach, which combines drilling and grinding, is a novel CTO-PCI procedure. This novel approach not only creates a hole in the calcified CTO lesion but also enlarges the lumen to the desired size, facilitating subsequent angioplasty or stent implantation. Therefore, it effectively addresses both uncrossable and undilatable challenges encountered in a single procedure.

The miniature Ni-diamond wheel (Fig. 4) was electroplated at one end of the drive shaft. The electroplating method was described in our previous study [42]. The drive shaft is approximately 1300 mm long and is made of three turns of 0.16-mm-diameter coils with an outer diameter of 0.65 mm. The other end of the drive shaft is connected to a motor to drive the high-speed rotation of the wheel. The miniature wheel is approximately 0.85 mm in diameter and 6 mm long. The average size of the diamond grit is 30 μm, with a grit distribution density of 38 per 260 μm×260 μm and an average grit height of 8 μm on the wheel surface [42].

2.2 Experimental setup

The experimental setup (Fig. 5) comprised five modules: (1) atherectomy device, (2) calcified CTO surrogate, (3) saline delivery system, (4) force measurement, and (5) wheel motion measurement. The five modules are detailed and discussed in the following subsections.

2.2.1 Atherectomy device

The atherectomy device comprises three units: (1) a catheter, (2) a motor and linear actuator, and (3) a motion controller.

The catheter consists of a drive shaft, diamond wheel, guidewire, and sheath (Fig. 4a). The 0.23-mm-diameter guidewire is made of stainless steel and extends from the atherectomy device via the hollow drive shaft and diamond wheel beyond the calcified CTO surrogate (Figs. 4 and 5). A guidewire lock fixes the guidewire from rotation and translation. During drilling and grinding, the wheel, driven by the drive shaft, rotates around and oscillates translationally along the guidewire. The guidewire extends from the CTO surrogate by 25 mm. The sheath is a thin plastic tube with a drive shaft rotating inside without direct contact with the vessel wall. Saline is pumped by a saline pump and flows inside the sheath and drive shaft for lubrication and frictional heat removal.

The direct current motor rotated the drive shaft from 12 000 to 116 000 r/min. The motor and catheter are on a linear rail and can be translated either by hand or by a linear actuator (Moog Animatics, Model HLD60, Santa Clara, CA, USA). The linear actuator (the upper right panel of Fig. 5) controls the oscillatory translational motion of the miniature wheel so that it oscillates and advances along the guidewire.

2.2.2 CTO surrogates

Obtaining human CTO lesions or developing animal CTO models is challenging, making it difficult to conduct preclinical testing and validation of new devices. Thus, artificial CTO models are commonly used [43]. Duer et al. [44] and Riel et al. [45] analyzed the mechanical properties of calcified plaques extracted from occluded arteries and found that these plaques resemble the formation, mineral composition, and hardness of bones. Thus, plaster and bovine bones are frequently used as surrogate materials for artificial CTO [44, 45]. Zheng et al. [46], Li et al. [47], and Lyu et al. [42] used plaster as a surrogate to test RA devices, whereas Liu et al. [48], Shih et al. [49], Zhu et al. [50], and Gao et al. [51] used bovine bones as surrogates for RA-related research. In the present study, CTO surrogates made of two materials, gypsum cement

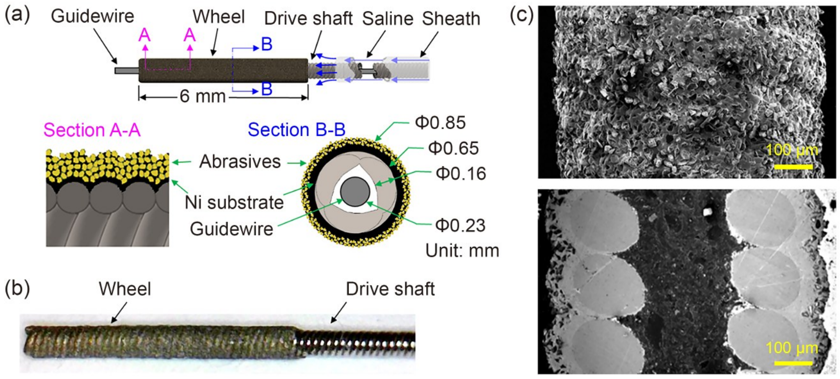

Fig. 4 Schematic of catheter, miniature diamond wheel (a) and wheel obtained via electroplating (b). (c) Scanning electron microscope images of the surface and cross-section of the wheel

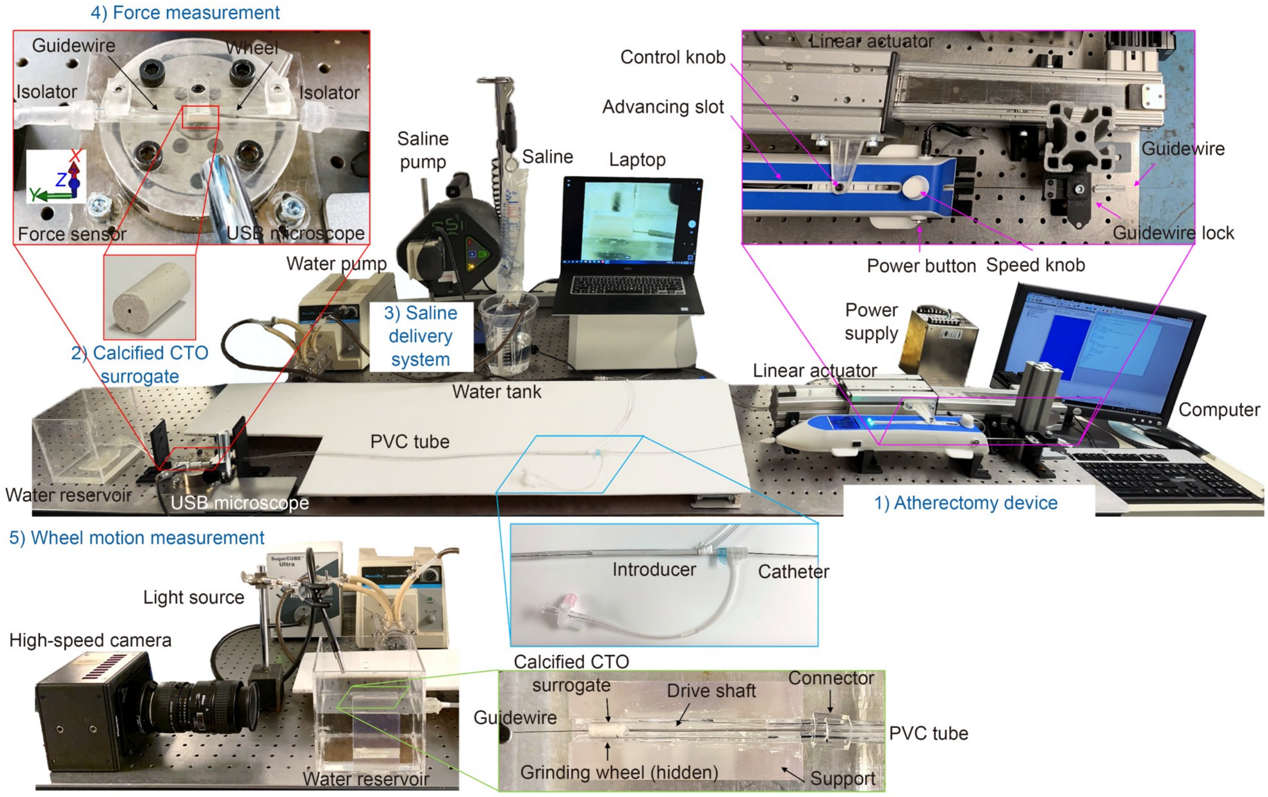

Fig. 5 Experimental setup for drilling and grinding of calcified CTO surrogate using a miniature diamond wheel

(Ultracal$^{®}$ 30, USG, Chicago, IL, USA) [52] and ex vivo bovine bone, were used to simulate the characteristics of calcified plaque in CTO drilling and grinding. The plaster was molded, and a 0.4-mm diameter hole was molded with a stainless steel wire as the core in the plaster surrogate. The bovine bone was cut into a 4-mm-long and 4-mm-diameter cylinder, and a 0.4-mm-diameter hole was drilled in the center. As shown in Fig. 5, the CTO surrogate was inserted inside a polyvinyl chloride (PVC) tube with an inner diameter of 4 mm and an outer diameter of 6 mm to simulate a severely calcified CTO lesion within a coronary artery.

2.2.3 Saline delivery system

Saline was used as the blood-mimicking fluid [53]. A roller pump was used to generate pulsatile pressure and flow in the PVC tube. An introducer (Super Sheath, Boston Scientific, Marlborough, MA, USA) was used to create an intervention entrance in the PVC tube for the catheter. As shown in the upper left of Fig. 5, the CTO surrogate was secured in a segment of the PVC tube on top of a dynamometer (Model Gamma SI-32-2.5, ATI Industrial Automation Inc., Apex, NC, USA). This segment has thin (0.5 mm in thickness) silicone-molded isolators on both sides [53]. The isolators isolate the force measurement unit from the tube on both sides, thereby avoiding the influence of the pulsatile pressure of the flow.

2.2.4 Force and wheel motion measurements

The three-axis force dynamometer simultaneously measures the forces in the x, y, and z directions at a sampling rate of 1000 Hz. As shown in the force measurement setup in Fig. 5, the y direction represents the axial direction of the PVC tube, drive shaft, and miniature wheel, and the z direction is perpendicular to the dynamometer and parallel to the gravity direction. The force in the y direction is used to characterize the drilling process, whereas forces in the x and z directions are used to determine the grinding force on the xz plane to characterize the grinding process.

During grinding, a high-speed camera (FASTCAM-1024PIC, Photron, Tokyo, Japan) records the wheel motion from the front end of the surrogate at 4000 frames per second. A light-emitting diode light source (SugarCUBE Ultra by Ushio America) delivers a concentrated light beam to enhance the depth of the field and image quality. During drilling, a digital microscope camera (Model OT-HD, Opti-Tekscope LLC, Chandler, AZ, USA) is set up by the side of the CTO surrogate to provide real-time visual feedback of the wheel position.

2.3 Design of experiments

Three sets of experiments (Exps. I, II, and III) were conducted to evaluate the miniature wheel for drilling and grinding CTO surrogates.

2.3.1 Exp. I: drilling (manual mode)

Three diamond wheels, denoted as Wheels 1, 2, and 3, were electroplated with an average diameter of 0.85 mm and a standard deviation (SD) of 0.006 mm. Each miniature wheel was drilled through five plaster surrogates using manual oscillatory translational motion. In addition, Wheel 1 was used to drill through a single bovine bone surrogate using manual oscillation. The drilling force in the axial (y) direction was also measured. Images of the proximal and distal ends of the surrogates before and after drilling were recorded. In total, 15 plaster and 1 bone surrogates were drilled.

During drilling, the wheel was placed near the proximal end of the surrogate following the guidewire. Saline was pumped through the PVC tube to fill the entire surrogate. The rotational speed of the wheel was 20 000 r/min. The wheel performed oscillatory translational motion, moving back and forth to drill through the surrogate under manual control. The oscillating speed and advancing distance of the manual oscillation motion were based on the visual feedback of the microscope camera and the haptic feedback of the drilling resistance. The frequency of the oscillation motion was analyzed using the measured force data. The drilling stopped when the diamond wheel successfully crossed the surrogate.

2.3.2 Exp. II: drilling (automated mode)

Wheels 2 and 3 were used to drill surrogates with a linear stage that controlled the oscillatory translational motion in two modes (rapid and slow). The wheels performed periodic oscillatory motion in each mode. In rapid mode, the wheels moved forward by 3 mm, backward by 3 mm, forward by 3.02 mm, and then backward by 3 mm. This was a motion cycle with a cycle time of 0.67 s (1.5 Hz). In slow mode, the wheels moved forward by 3 mm, backward by 3 mm, forward by 3.0125 mm, and then backward by 3 mm. This was a motion cycle with a cycle time of 0.75 s (1.33 Hz). The wheels advanced once for every two oscillating movements. The average advancing speeds in the rapid and slow modes were 2 and 1 mm/min, respectively.

Both wheels were drilled through five plaster and one bone surrogates. The drilling forces in the y direction and images of the shapes of the holes at both ends of the surrogates were recorded. The wheel rotational speed and stop condition were the same as those in manual mode. In total, 10 plaster and 2 bone surrogates were drilled in the automated mode.

2.3.3 Exp. III: grinding (hole enlargement)

Wheels 1–3 were used to grind and enlarge the holes by orbital motion in the plaster and bone surrogates after Exps. I and II. The grinding force and wheel motion were measured. However, the grinding force and wheel motion could not be measured simultaneously because the tip of the diamond wheel, along with the CTO surrogate hole, must be exposed for the high-speed camera to observe wheel motion, which could not be measured when the wheel was embedded in the surrogate during the force measurement setup. For each wheel, three of the drilled plaster surrogates were selected and used to measure the grinding force. The other two plaster surrogates were used to observe the wheel motion during grinding. After grinding five plaster surrogates, Wheels 1–3 were used to grind a bone surrogate. Wheel 1 was used to observe the motion, and Wheels 2 and 3 were used to measure the force required to grind the bone surrogates.

Figure 5 shows the setup for measuring the grinding forces in the x and z directions and for observing the wheel motion using the high-speed camera. The tip of the diamond wheel was aligned with the distal end of the surrogates. The grinding duration was 120 s, and the rotational speed of the wheels was 20 000 r/min. During grinding, saline is flowed through the surrogate to mimic the flow of blood.

3 Experimental results

The results of Exps. I, II, and III are presented in the following three subsections.

3.1 Results of Exp. I: drilling (manual mode)

3.1.1 Diameter change

All 15 plaster surrogates as well as one bone surrogate in Exp. I were successfully drilled through. Figure 6 shows the proximal and distal ends of the plaster and bone surrogates before and after manual mode drilling by the three wheels.

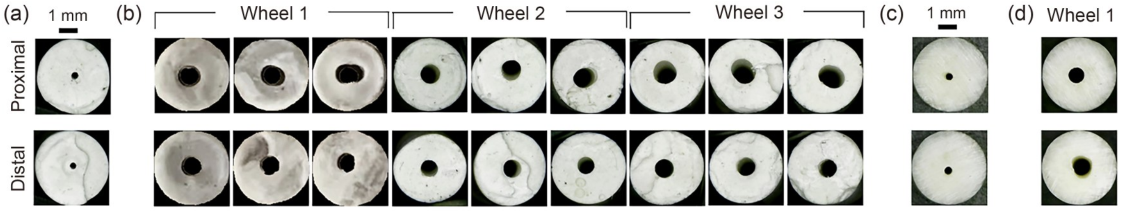

Fig. 6 Images of proximal and distal ends of surrogates: before (a) and after (b) manual drilling on plaster surrogates (Wheels 1–3), and before (c) and after (d) manual drilling on the bone surrogate (Wheel 1)

One of the plaster surrogates (with a 0.4-mm-diameter molded hole) before manual mode drilling and three of the five plaster surrogates after drilling are presented. As shown in Fig. 6b, the hole diameter in the plaster surrogates was increased to at least 0.85 mm (diameter of the miniature diamond wheel). The diameters of the proximal holes (top row) are larger than those at the distal end (bottom row). The diamond wheel and drive shaft had a longer contact time and exhibited orbital motion at the proximal end during drilling. The details of the wheel motion are discussed in Sect. 3.3.

For bone surrogate drilling using Wheel 1, the proximal and distal ends of the bone surrogate before and after manual drilling are shown in Figs. 6c and 6d, respectively. The wheel successfully drilled through the bone surrogate at approximately the same frequency (3 Hz) as that used in manual oscillatory drilling of the plaster surrogates.

3.1.2 Drilling force

The measured axial drilling forces along the y direction (Fig. 5) in manual mode and fast Fourier transform (FFT) analysis of the corresponding frequency are shown in Fig. 7. The results of one of the five plaster drilling tests for each wheel are presented as representative samples. The blue curves represent the raw force data, and the red curves represent the filtered data after applying a Butterworth low-pass filter with a cutoff frequency of 6 Hz. Figure 7b shows that an approximately 3-Hz frequency of the oscillation motion was controlled in manual mode. The average peak drilling forces calculated from the filtered data for the plaster surrogates of the three wheels are summarized in Table 1. The average peak drilling forces for Wheels 1, 2, and 3 were 0.085, 0.128, and 0.104 N, respectively, yielding an overall average peak force of 0.106 N with a small SD of 0.023 N. The drilling force for plaster surrogates was consistent for all three wheels.

The drilling force and frequency analysis results for bone surrogate drilling using Wheel 1 are presented in Fig. 7. The average peak drilling force (approximately 0.2 N) was significantly higher than that of plaster drilling (0.1 N). The results of plaster and bone surrogates demonstrate the consistency and feasibility of miniature diamond wheels in manual mode for drilling holes in totally occluded and calcified CTO lesions.

3.2 Results of Exp. II: drilling (automated mode)

3.2.1 Diameter change

The drilling results for both the plaster and bone surrogates using Wheel 2 in rapid mode and Wheel 3 in slow mode in automated drilling are presented in Fig. 8. For plaster drilling, Fig. 8a shows the shape of the proximal end (top row)

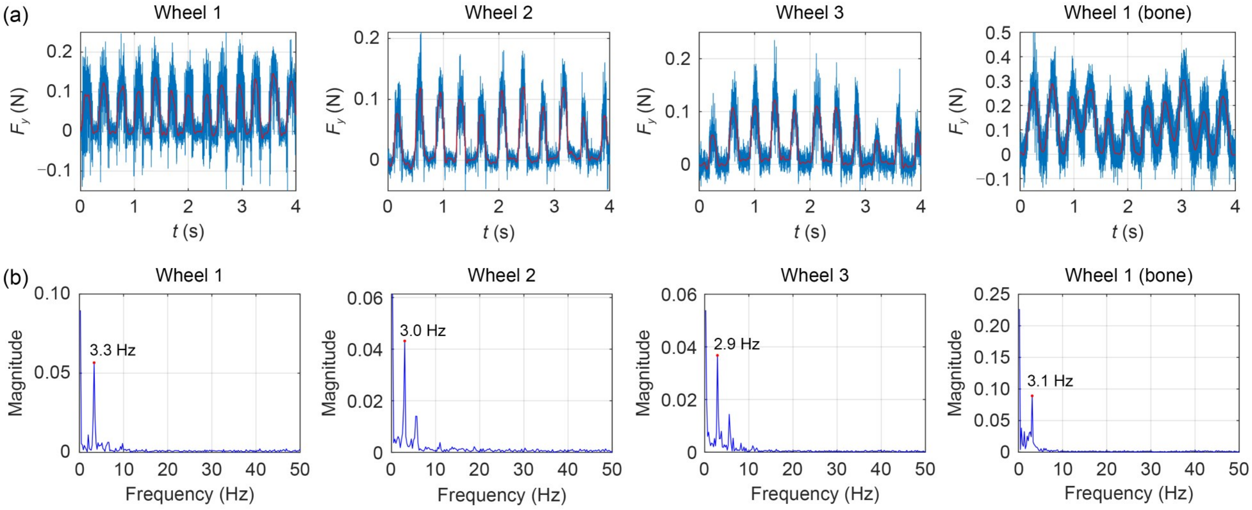

Fig. 7 Manual drilling: (a) measured force (blue) and filtered force (red) data of three wheels on plaster surrogates and Wheel 1 on the bone surrogate; (b) corresponding frequency domain analysis

Table 1 Average peak drilling forces of manual drilling on plaster surrogates (unit: N)

	Plaster 1	Plaster 2	Plaster 3	Plaster 4	Plaster 5	Average	SD
Wheel 1	0.083	0.067	0.073	0.084	0.115	0.085	0.018
Wheel 2	0.131	0.140	0.136	0.136	0.097	0.128	0.018
Wheel 3	0.137	0.091	0.109	0.101	0.085	0.104	0.020
Overall	–	–	–	–	–	0.106	0.023

and distal end (bottom row) of the hole drilled in the plaster surrogates. Similar to the hole shapes shown in Fig. 6b, the size is larger at the proximal end because of the longer duration of wheel contact during drilling using a diamond wheel with oscillatory motion. For bone drilling, such size differences at the proximal and distal ends (Fig. 8b) are less significant. This is likely due to the less orbital motion with more stable oscillatory motion in the automated mode. The hole size was slightly larger in the slow mode than in the rapid mode. Compared with the manual mode (Fig. 6), the automated mode resulted in no significant difference in hole shape after drilling. The wheels successfully drilled through the bone surrogates in both rapid and slow automated modes.

3.2.2 Drilling force

The automated mode drilling forces and the corresponding frequency analysis results are presented in Fig. 9. One of the five drilling tests for the plaster surrogates and the bone drilling tests for Wheels 2 and 3 are presented. The average peak drilling forces for the plaster surrogates in the two automated modes are summarized in Table 2. For plaster surrogate drilling, the average peak drilling forces in the rapid and slow automated modes were 0.046 and 0.027 N, respectively, at the same oscillation frequency of 3 Hz. For bone surrogate drilling, the drilling forces in the rapid and slow automated modes were almost the same (approximately 0.1 N). This value is higher than the values of 0.027 N (slow mode) and 0.046 N (rapid mode) obtained for drilling the plaster surrogates. Overall, the drilling force was smaller in the automated mode than in the manual mode regardless of the surrogate material.

In the rapid automated mode drilling of the plaster surrogates, the forces recorded for plasters 1 and 3 were significantly higher than those recorded for plasters 2, 4, and 5 (Table 2). For the latter three plasters, the drilling forces in

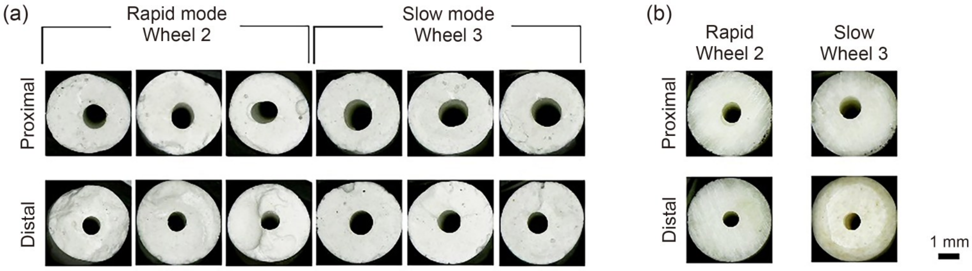

Fig. 8 Images of proximal and distal ends of plaster (a) and bone (b) surrogates after drilling in automated mode

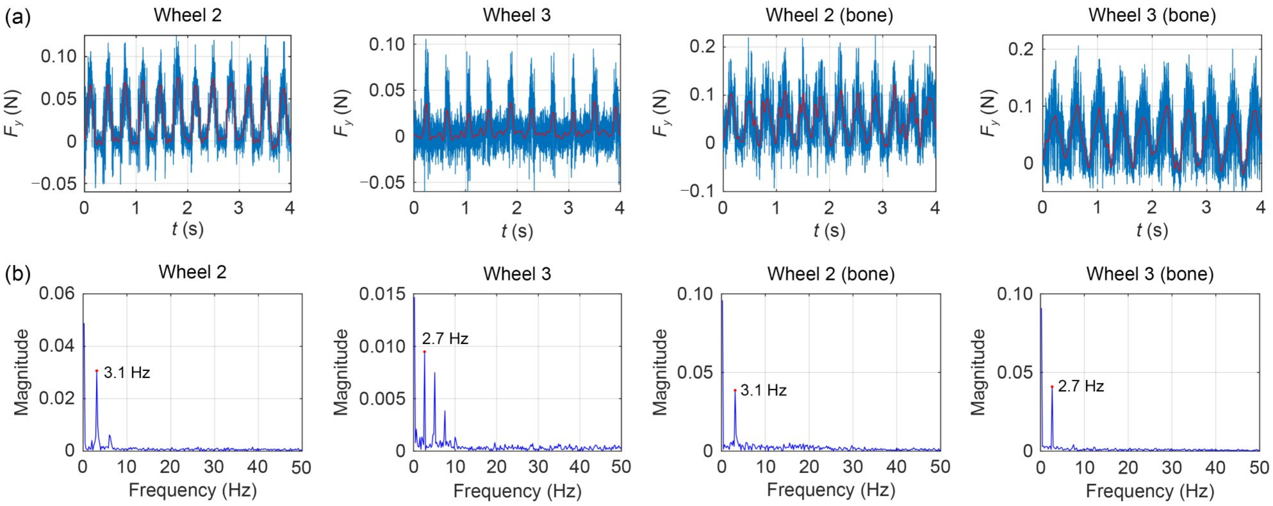

Fig. 9 Measured drilling force in automated mode: (a) measured force (blue) and filtered force (red) data obtained from automated drilling of plaster and bone surrogates; (b) corresponding frequency domain analysis

Table 2 Average peak drilling forces of automated drilling on plaster surrogates (unit: N)

Automated mode	Plaster 1	Plaster 2	Plaster 3	Plaster 4	Plaster 5	Average	SD
Rapid mode	0.069	0.027	0.083	0.025	0.024	0.046	0.028
Slow mode	0.015	0.031	0.032	0.025	0.032	0.027	0.008

the rapid mode were comparable to those observed in the slow mode. Given that the bone surrogate exhibited similar peak forces in both modes, it could be inferred that the two automated modes produced generally comparable force levels. In each cycle, due to the flexibility of the drive shaft, a higher advancing distance in the rapid mode did not increase the depth of drilling and grinding; thus, the cutting force did not increase. However, a higher advancing distance increased the contact and grinding time (duration of the force peak), as demonstrated by the comparison between Wheels 2 and 3 in Fig. 9a. This extended grinding time aligns with the higher material removal rate in the rapid mode. The elevated forces recorded for plasters 1 and 3 in the rapid mode may be due to material inconsistencies or guidewire misalignment, which can cause the wheel axis to deviate from parallel alignment with the surrogate axis.

3.3 Results of Exp. III: grinding (hole enlargement)

3.3.1 Wheel motion

All holes in the plaster and bone surrogates in Exp. III were successfully enlarged by grinding. During 120 s of grinding, the hole continued to enlarge. The motion pattern of the wheel changed depending on the hole diameter. Two motion patterns, semi-orbital and orbital motions, of the wheel were observed in Periods I and II, respectively, during the grinding process. Figure 10a shows an example of wheel positions versus time in Period I with semi-orbital motion at the beginning of the grinding process. The wheel bounced on the left side of the hole. Only half of the inner wall of the surrogate was touched and ground. The wheel completed a semi-orbital cycle in 0.003 s at a wheel rotational speed of 20 000 r/min. This is likely due to the slightly curved guidewire, which is discussed in Sect. 4. As the hole size expanded, the motion pattern of the wheel changed to orbital motion in Period II. An example of the orbital motion is shown in Fig. 10b. The rotating diamond wheel orbits in the inner wall of the hole. The period for each orbiting cycle for all plaster surrogates was approximately the same (0.006 s), corresponding to an orbital speed of 10 000 r/min, which is approximately half the rotational speed of the wheel. This orbital speed is high because the lumen size is small but slightly larger than that of the diamond wheel.

The criterion for distinguishing Period I from Period II is whether the diamond wheel made full revolutions along the inner wall of the hole. The hole diameter at which the wheel started to orbit ranged from 0.96 to 1.09 mm in different plaster surrogates, with an average diameter of 1.04 mm to start the transition from semi-orbital to orbital motion. Among the six plaster surrogates used for motion observation in Exp. III, orbital motions were observed in five of them within 120 s. The remaining plaster surrogate exhibited orbital motion after over 120 s of semi-orbital motion of the diamond wheel.

3.3.2 Diameter change

Images of the distal ends of the plaster and bone surrogates after 120 s of grinding are shown in Fig. 11. The hole diameters of the plaster surrogates ranged from 1.04 to 1.56 mm,

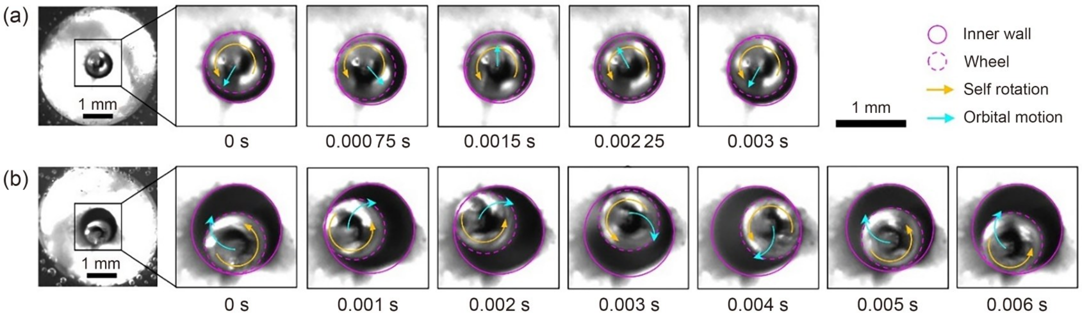

Fig. 10 Wheel motion patterns during grinding: (a) semi-orbital motion (one cycle) in Period I (the wheel does not contact the right side of the inner wall); (b) orbital motion in Period II (full cycle circular orbital motion observed)

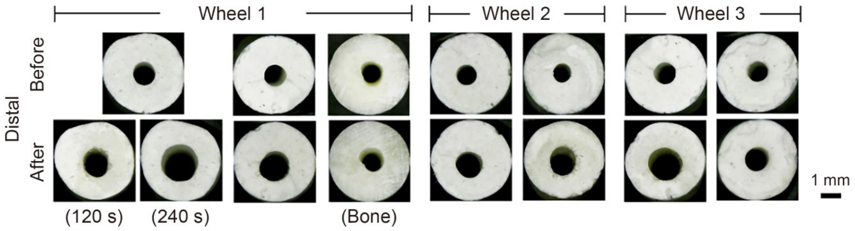

Fig. 11 Images of distal ends of plaster and bone surrogates after 120 s of grinding

with an average diameter of 1.26 mm after 120 s of grinding. For the bone surrogate, the hole expanded to 1.06 mm after 120 s of grinding. Orbital motion was not observed in the bone surrogate within 120 s during the motion observation experiments because the required hole diameter for generating orbital motion was not achieved. However, wheel orbital motion within the bone surrogates was detected in the force measurement experiments via frequency domain analysis.

3.3.3 Contact force

The contact forces of the three grinding wheels were measured in the *x* and *z* directions based on the force measurement setup shown in Fig. 5. To exclude the effect of gravity, contact forces in the *x* direction (F_x) and the corresponding FFT frequency analysis of grinding on the plaster and bone surrogates for Periods I and II are presented in Fig. 12. The contact force in Period II was slightly smaller than that in Period I. The wheel rotation frequencies (351.9, 348.4, 339.2, and 337.2 Hz) in the frequency domain for Periods I and II are shown in Figs. 12e–12h. The wheel rotational speeds were close to 20 000 r/min. The 174.5- and 178.7-Hz components in Figs. 12f and 12h correspond to wheel orbital speeds of 10 470 and 10 722 r/min. The semi-orbital is equal to the self-rotational speed of the diamond wheel; thus, the frequency of the semi-orbital motion cannot be distinguished. The 56.6-, 43.7-, 18.2-, and 11.5-Hz peaks in Figs. 12e–12h may have been caused by fluid and rotating debris in saline driven by the wheel. This low frequency differs between the plaster and bone samples and can be attributed to the difference in friction on the inner surface of the materials. This phenomenon is yet to be investigated.

Table 3 summarizes the peak contact force in the *x* direction of plaster surrogate grinding for all three wheels. The grinding force is slightly smaller in Period II than in Period I. This result is consistent with the results presented in Fig. 12. The average grinding forces of Wheels 1, 2, and 3 on the plaster surrogates were 0.046, 0.042, and 0.036 N, respectively. The overall average peak contact force was 0.041 N. The grinding forces of the three wheels on the plaster surrogates are consistent. The grinding force on the bone surrogates was slightly smaller than that on the plaster surrogates (Fig. 12). This was likely due to the smooth inner surface of the bone surrogate.

4 Discussions

This study proposed an atherectomy method for CTO-PCI based on sequential drilling and grinding of classified plaques

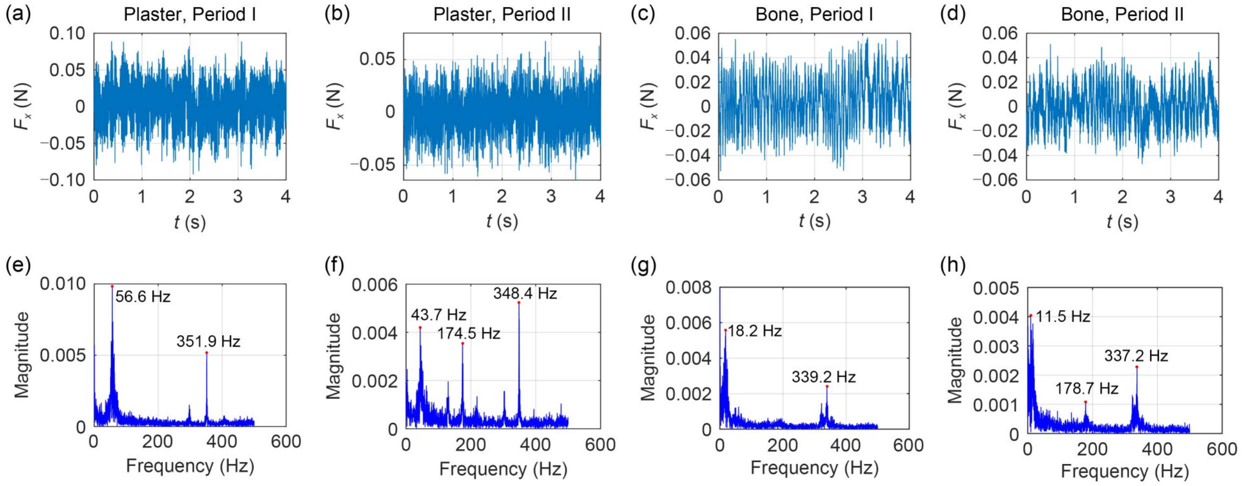

Fig. 12 Contact force in the *x* direction vs. time in Period I (a) and Period II (b) of plaster surrogate grinding, and in Period I (c) and Period II (d) of bone surrogate griding. Frequency analysis of force in Period I (e) and Period II (f) of plaster surrogate grinding, and in Period I (g) and Period II (h) of bone surrogate grinding

Table 3 Average contact forces in the *x* direction and the SDs of three wheels during plaster surrogate grinding (unit: N)

	Plaster 1 Period I	Plaster 1 Period II	Plaster 2 Period I	Plaster 2 Period II	Plaster 3 Period I	Plaster 3 Period II	Average	SD
Wheel 1	0.065	0.029	0.055	0.036	0.054	0.036	0.046	0.014
Wheel 2	0.019	0.048	0.035	0.023	0.083	0.044	0.042	0.023
Wheel 3	0.029	0.035	0.022	0.024	0.084	0.022	0.036	0.024
Overall	–	–	–	–	–	–	0.041	0.019

using a sub-mm Ni-diamond wheel. Experiments were conducted to verify the feasibility of the proposed device and to analyze the effects of changes in the surrogate size and wheel drilling and grinding forces.

During drilling, the drilling force in the manual mode (0.106 N) was significantly higher than that in the automated mode (0.027 and 0.046 N in slow and rapid modes, respectively). The shape of the holes after drilling under different oscillatory translational motion patterns was the same (Figs. 6 and 8). These results indicate more consistent and potentially better drilling in the automated mode. The reason for the decrease in the drilling force was that the automated oscillatory translational motion was more consistent in terms of frequency and displacement. Manual mode drilling can be aggressive under feedback from haptic sensing, audio (motor and grinding), and visualization of the wheel location. Manual wheel oscillation is common in current atherectomy procedures. In addition, in the automated mode, real-time monitoring and display of motor torque can be achieved and used as feedback to assist interventionists with manual control of drilling in CTO treatment. This result suggests a potential approach to reducing drilling force while improving consistency. The automated feeding method has not been used in hospitals, and no previous studies have investigated the impact of motion patterns.

Orbital grinding was used to expand the lumen diameter of the wheel drill through the CTO surrogates. Grinding with orbital motion is preferred because it removes plaques more uniformly around the lumen. Existing studies have indicated that orbital motion is caused by hydraulic forces: a high-speed rotating grinding wheel drives the surrounding fluid to form laminar flow and vortices, thereby forming different pressure zones on both sides of the contact point between the wheel and inner wall [54]. The pressure difference causes the grinding wheel to orbit around the inner wall. In this study, the semi-orbital motion of the diamond wheel was observed at the start of the grinding: the wheel bounced partially along the inner wall rather than in a full circle (Fig. 10a). At the start, the diameters of the hole and wheel are almost the same (0.85 mm), and the thickness of the liquid film around the wheel is small, resulting in a low hydraulic force that cannot support the orbital motion of the wheel. In addition, the drive shaft may contact the inner wall, and the axis of the guidewire may not align perfectly with that of the hole. The misalignment between the axes of the guidewire and the hole causes the wheel to grind on one side and return the guidewire to a straight state with the expansion of the hole size. Once the axes of the hole and wheel are aligned and the thickness of the liquid film increases, the hydraulic force increases, and the wheel begins to perform full orbital motion [54]. According to the experimental results, this transition from semi-orbital to full orbital motions typically occurs within 60–90 s of grinding when the lumen diameter exceeds approximately 1.04 mm. In future research, the grinding theory and fluid mechanics theory can be combined to model the dynamics of the grinding wheel, and the conditions for orbital motion and motion pattern transition can be explored. In addition, orbital grinding was performed for only 120 s in this study. The lumen diameter can continue to increase with continuous grinding; however, a threshold should be established. The investigation of the threshold of orbital grinding under different conditions is also a future research direction.

To the authors' best knowledge, no reference data on crossing calcified CTO lesions by drilling are available. Thus, it is difficult to fully justify the force measured while drilling calcified CTO surrogates. For grinding, Zheng et al. [52, 53] experimentally measured the grinding forces using Boston Scientific's RA device and Diamondback's 360® orbital atherectomy (OA) device. The grinding force on calcified plaque surrogates using OA ranges from 0.1 to 0.4 N [52], whereas the force using RA ranges from 0.10 to 0.25 N [49, 53]. As shown in Table 3, the grinding force of the miniature wheel was only 0.041 N, which is lower than that of existing devices. This is a key advantage because the lower force reduces heat and the risk of complications. Zheng et al. [54] also found that the grinding force is positively correlated with wheel diameter, and smaller wheels exert lower forces than larger wheels. The smaller wheel size is the primary reason for the reduced force observed in this study.

Problems were then observed in our experiments. If there is excessive misalignment between the axes of the guidewire and the surrogate hole, the wheel may fail to generate orbital motion during grinding. Figure 13 illustrates a case in which a large angle (3°) exists between the guidewire and hole axes. As shown in Fig. 13a, the diamond wheel ground translationally to the left side during 120 s of local grinding. Images of the distal ends of the plaster surrogates after such 120 s of grinding on one side are shown in Fig. 13b. In practice, blood vessels generally have curved geometry, which

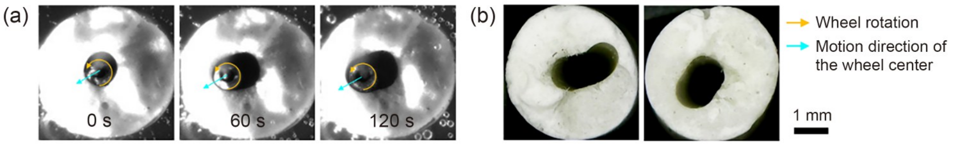

Fig. 13 Effect of misalignment of guidewire and hole axes: (a) translational wheel motion pattern observed during local grinding; (b) distal ends of CTO surrogates after local grinding

inevitably leads to misalignment between the axes of the guidewire and blood vessels. The phenomenon of translational wheel motion or semi-orbital motion occurs during blood vessel grinding. To overcome this problem, an eccentric wheel design can be considered. When an eccentric wheel rotates at a high speed, a centrifugal force is generated, which assists the wheel in performing full-circle orbital motion. In future studies, we plan to use the proposed wheel to grind curved artery surrogates.

Safety is a critical concern in medical device development. In PCI using RA, complications such as vascular dissection, slow/no reflow, distal vessel obstruction, and myocardial infarction may occur [50]. Research has demonstrated that the complications associated with RA may be related to factors such as grinding force, thermal damage, and debris size [50]. Although the present study does not directly verify the safety of the proposed method using in vivo or animal experiments, several indirect indicators suggest its potential safety. As previously mentioned, the grinding force of the miniature wheel is significantly lower than that of existing RA devices. In addition, the orbital motion of the miniature wheel helps remove plaques more uniformly around the lumen, thereby reducing the risk of artery perforation and promoting heat dissipation by avoiding grinding at the same location for a long period. This approach protects blood vessels from thermal injury and blood coagulation. Regarding debris size, debris smaller than 30 μm is generally considered safe [55]. Liu et al. [56] and Zheng et al. [57] investigated the surface morphology and debris size generated during grinding using Boston Scientific's RA device. They found that 90% of the debris generated by RA grinding was smaller than 30.87 μm. The grit heights of RA devices used in previous research range from 0.6 to 10.5 μm [56, 57]. The average grit height of the miniature wheel used in this study is 8 μm [42], which falls within the range reported by Liu and Zheng et al. [56, 57]. Given the comparable grit size, the reduced grinding force and smaller wheel size in the proposed method are likely to further decrease the debris particle size, which we plan to validate in future work.

Compared to existing solutions for microcatheter- and balloon-uncrossable CTO lesions, including BAM, ELCA, and RA, the proposed approach has notable advantages. (1) Smallest tool size: the tool sizes of the currently used BAM, ELCA, and RA devices are in ranges of 1.2–1.5 mm [39], 0.9–2.0 mm [40], and 1.25–2.50 mm [41], respectively, whereas the miniature wheel used in this study is only 0.85 mm, allowing it to access smaller arteries more easily. (2) Effectiveness for high-hardness CTO lesions: unlike BAM and ELCA, which are unsuitable for highly calcified lesions, the proposed approach is effective for high-hardness CTO lesions. (3) Two-in-one procedure with sequential drilling and grinding: the proposed approach not only creates a hole in a hardened CTO lesion but also expands the lumen size through orbital grinding, potentially solving the undilatable lesion problem and saving time during subsequent angioplasty or stent implantation. Furthermore, the lower force and orbital motion involved in this process make the proposed miniature diamond wheel safer than the currently used RA devices.

The proposed system is the first atherectomy device designed for CTO-PCI that uses a sub-mm miniature diamond wheel to initially drill the target lesion and then enlarge the lumen size through orbital grinding. The experimental results strongly demonstrate the potential of the proposed atherectomy method to successfully cross CTO lesions, where existing approaches may fail. The experimental results provide confidence that the proposed technology can significantly contribute to the treatment of complex, uncrossable CTO lesions. Further studies are required to improve the proposed device. For example, the wheel length or arrangement can be adjusted according to the presence of different lesions. In addition, thermal analysis, motion and force modeling, debris size collection, and analysis can further elucidate the characteristics of the proposed method. CTO lesions harvested from real patients can be used to further verify the effectiveness of the proposed method.

5 Conclusions

This study explored a new approach for overcoming the clinical challenges of microcatheter- and balloon-uncrossable lesions in CTO-PCI. The performances of miniature Ni-diamond electroplated wheels were investigated by drilling and grinding calcified CTO surrogates made of plaster and bovine bone materials. The experimental results quantitatively and qualitatively verified the drilling and grinding feasibility and forces of the miniature wheel. During drilling, the miniature wheel successfully drills through the plaster and bone surrogates in both manual and automated modes to create a hole of approximately 0.85 mm in diameter (the size of the wheel). A lower and more consistent drilling force indicates the potential of automated drilling in CTO treatment. After penetrating the calcified CTO surrogates, the diamond wheel further enlarged the hole by grinding. Semi-orbital motion was observed at the beginning of the grinding process, likely caused by limited liquid film thickness and axial misalignment between the guidewire and surrogate hole. As the grinding progressed, the axial alignment improved and the liquid film thickened, enabling the transition to full orbital motion of the wheel. The orbital motion of the wheel enlarged the hole. After 120 s of grinding, the hole diameter of the plaster CTO surrogates increased to 1.26 mm on average, which resolved the microcatheter- and balloon-uncrossable problems. The results of this study lay the foundation for future research on device development and modeling of material removal mechanisms for calcified CTO lesions. The limitations of this study include the single material composition and straight geometry of the calcified CTO surrogate, and only one rotational speed was used for drilling and grinding. Future studies will address these limitations and conduct experiments on calcified CTO lesions harvested from human subjects. Future research topics include drilling and grinding models for the calculation and analysis of machining forces and torques and computational fluid dynamics studies on the causes of orbital motion.

Author contributions ZZ was involved in conceptualization, investigation, methodology, and writing—original draft. JJL was involved in investigation, methodology, and writing—original draft. YZ was involved in methodology and writing—review & editing. HSG and AJS were involved in conceptualization, supervision, and writing—review & editing.

Declarations

Conflict of interest The authors declare that they have no conflict of interest.

Ethical approval This study does not contain any studies with human or animal subjects performed by any of the authors.

Data availability The data that support the findings of this study are available from the corresponding author upon reasonable request.

References

1. Jeroudi OM, Alomar ME, Michael TT et al (2014) Prevalence and management of coronary chronic total occlusions in a tertiary veterans affairs hospital. Catheter Cardiovasc Interv 84(4):637–643. https://doi.org/10.1002/ccd.25264
2. Shin SH, Baril D, Chaer R et al (2011) Limitations of the Outback LTD re-entry device in femoropopliteal chronic total occlusions. J Vasc Surg 53(5):1260–1264. https://doi.org/10.1016/j.jvs.2010.10.127
3. Chi WK, Gong MQ, Bazoukis G et al (2018) Impact of coronary artery chronic total occlusion on arrhythmic and mortality outcomes: a systematic review and meta-analysis. JACC Clin Electrophysiol 4(9):1214–1223. https://doi.org/10.1016/j.jacep.2018.06.011
4. Smith EJ, Strange JW, Hanratty CG et al (2013) Percutaneous intervention for chronic total occlusion: integrating strategies to address an unmet need. Heart 99(20):1471–1474. https://doi.org/10.1136/heartjnl-2013-304521
5. Srinivas VS, Brooks MM, Detre KM et al (2002) Contemporary percutaneous coronary intervention versus balloon angioplasty for multivessel coronary artery disease: a comparison of the National Heart, Lung and Blood Institute Dynamic Registry and the Bypass Angioplasty Revascularization Investigation (BARI) study. Circulation 106(13):1627–1633. https://doi.org/10.1161/01.cir.0000031570.27023.79
6. Werner GS, Gitt AK, Zeymer U et al (2009) Chronic total coronary occlusions in patients with stable angina pectoris: impact on therapy and outcome in present day clinical practice. Clin Res Cardiol 98(7):435–441. https://doi.org/10.1007/s00392-009-0013-5
7. Claessen BEPM, Hoebers LP, van der Schaaf RJ et al (2010) Prevalence and impact of a chronic total occlusion in a non-infarct-related artery on long-term mortality in diabetic patients with ST elevation myocardial infarction. Heart 96(24):1968–1972. https://doi.org/10.1136/hrt.2010.197673
8. Fefer P, Knudtson ML, Cheema AN et al (2012) Current perspectives on coronary chronic total occlusions the Canadian multicenter chronic total occlusions registry. J Am Coll Cardiol 59(11):991–997. https://doi.org/10.1016/j.jacc.2011.12.007
9. Stein JH, Weiss MB, Ro JH et al (1984) Percutaneous transluminal coronary angioplasty of a coronary artery with a total occlusion. Arch Intern Med 144(9):1875–1877
10. Wang CY (2017) TCTAP C-109 successful PCI of a heavy calcified LAD CTO lesion by antegrade parallel wiring technique with rotablator rotational atherectomy. J Am Coll Cardiol 69(16): S198–S199. https://doi.org/10.1016/j.jacc.2017.03.337
11. Othman H, Seth M, Zein R et al (2020) Percutaneous coronary intervention for chronic total occlusion: the Michigan experience insights from the BMC2 registry. JACC Cardiovasc Interv 13(11):1357–1368. https://doi.org/10.1016/j.jcin.2020.02.025
12. Grantham JA, Jones PG, Cannon L et al (2010) Quantifying the early health status benefits of successful chronic total occlusion recanalization: results from the FlowCardia's Approach to Chronic Total Occlusion Recanalization (FACTOR) trial. Circ Cardiovasc Qual Outcomes 3(3):284–290. https://doi.org/10.1161/CIRCOUTCOMES.108.825760
13. Joyal D, Afilalo J, Rinfret S (2010) Effectiveness of recanalization of chronic total occlusions: a systematic review and meta-analysis. Am Heart J 160(1):179–187. https://doi.org/10.1016/j.ahj.2010.04.015
14. Kirschbaum SW, Baks T, van den Ent M et al (2008) Evaluation of left ventricular function three years after percutaneous recanalization of chronic total coronary occlusions. Am J Cardiol 101(2):179–185. https://doi.org/10.1016/j.amjcard.2007.07.060
15. Nombela-Franco L, Mitroi CD, Fernández-Lozano I et al (2012) Ventricular arrhythmias among implantable cardioverter-defibrillator recipients for primary prevention: impact of chronic total coronary occlusion (VACTO Primary Study). Circ Arrhythm Electrophysiol 5(1):147–154. https://doi.org/10.1161/CIRCEP.111.968008
16. Christakopoulos GE, Christopoulos G, Carlino M et al (2015) Meta-analysis of clinical outcomes of patients who underwent percutaneous coronary interventions for chronic total occlusions. Am J Cardiol 115(10):1367–1375. https://doi.org/10.1016/j.amjcard.2015.02.038

17. Azzalini L, Carlino M, Bellini B et al (2020) Long-term outcomes of chronic total occlusion recanalization versus percutaneous coronary intervention for complex non-occlusive coronary artery disease. Am J Cardiol 125(2):182–188. https://doi.org/10.1016/j.amjcard.2019.10.034
18. Tajti P, Karmpaliotis D, Alaswad K et al (2018) The hybrid approach to chronic total occlusion percutaneous coronary intervention: update from the PROGRESS CTO registry. JACC Cardiovasc Interv 11(14):1325–1335. https://doi.org/10.1016/j.jcin.2018.02.036
19. Brilakis ES, Mashayekhi K, Burke MN (2019) How DECISION-CTO can help guide the decision to perform chronic total occlusion percutaneous coronary intervention. Circulation 139(14): 1684–1687. https://doi.org/10.1161/CIRCULATIONAHA.119.039835
20. Brilakis ES, Banerjee S, Karmpaliotis D et al (2015) Procedural outcomes of chronic total occlusion percutaneous coronary intervention a report from the NCDR (National Cardiovascular Data Registry). JACC Cardiovasc Interv 8(2):245–253. https://doi.org/10.1016/j.jcin.2014.08.014
21. Kiesz RS, Rozek MM, Ebersole DG et al (1999) Novel approach to rotational atherectomy results in low restenosis rates in long, calcified lesions: long-term results of the San Antonio rotablator study (SARS). Catheter Cardiovasc Interv 48(1):48–53. https://doi.org/10.1002/(SICI)1522-726X(199909)48:1<48::AID-CCD9>3.0.CO;2-Y
22. Hoffmann R, Mintz GS, Kent KM et al (1998) Comparative early and nine-month results of rotational atherectomy, stents, and the combination of both for calcified lesions in large coronary arteries. Am J Cardiol 81(5):552–557. https://doi.org/10.1016/S0002-9149(97)00983-1
23. Morino Y, Abe M, Morimoto T et al (2011) Predicting successful guidewire crossing through chronic total occlusion of native coronary lesions within 30 minutes: the J-CTO (multicenter CTO registry in Japan) score as a difficulty grading and time assessment tool. JACC Cardiovasc Interv 4(2):213–221. https://doi.org/10.1016/j.jcin.2010.09.024
24. Suzuki Y, Tsuchikane E, Katoh O et al (2017) Outcomes of percutaneous coronary interventions for chronic total occlusion performed by highly experienced Japanese specialists: the first report from the Japanese CTO-PCI expert registry. JACC Cardiovasc Interv 10(21):2144–2154. https://doi.org/10.1016/j.jcin.2017.06.024
25. Fang HY, Lee CH, Fang CY et al (2011) Application of penetration device (Tornus) for percutaneous coronary intervention in balloon uncrossable chronic total occlusion: procedure outcomes, complications, and predictors of device success. Catheter Cardiovasc Interv 78(3):356–362. https://doi.org/10.1002/ccd.22862
26. Dash D (2016) Guidewire crossing techniques in coronary chronic total occlusion intervention: A to Z. Indian Heart J 68(3):410–420. https://doi.org/10.1016/j.ihj.2016.02.019
27. Rossi JE, Nair R, Ellis SG et al (2020) Use of polymer-jacketed, tapered-tip, low-force guidewires with composite-core, dual-coil design as part of the antegrade approach to coronary chronic total occlusions. J Invasive Cardiol 32(5):161–168. https://doi.org/10.25270/jic/19.00495
28. Michael TT, Papayannis AC, Banerjee S et al (2012) Subintimal dissection/reentry strategies in coronary chronic total occlusion interventions. Circ Cardiovasc Interv 5(5):729–738. https://doi.org/10.1161/CIRCINTERVENTIONS.112.969808
29. Masoomi R, Boukhris M, Moscardelli S et al (2024) Dissection and re-entry techniques for chronic total occlusion percutaneous coronary intervention. Interv Cardiol 19:e16. https://doi.org/10.15420/icr.2024.04
30. Green P, Monga S, Ramcharitar S et al (2016) Tools and techniques–clinical update on coronary guidewires 2016: chronic total occlusions. EuroIntervention 11(9):1077–1079. https://doi.org/10.4244/eijv11i9a216
31. Pigott JP, Raja ML, Davis T (2012) A multicenter experience evaluating chronic total occlusion crossing with the Wildcat catheter (the CONNECT study). J Vasc Surg 56(6):1615–1621. https://doi.org/10.1016/j.jvs.2012.06.071
32. Ge JB, Ge L, Huo Y et al (2021) Updated algorithm of chronic total occlusion percutaneous coronary intervention from chronic total occlusion club China. Cardiol Plus 6(2):81–87. https://doi.org/10.4103/2470-7511.320320
33. Karacsonyi J, Karmpaliotis D, Alaswad K et al (2017) Prevalence, indications and management of balloon uncrossable chronic total occlusions: insights from a contemporary multicenter US registry. Catheter Cardiovasc Interv 90(1):12–20. https://doi.org/10.1002/ccd.26780
34. Tajti P, Karmpaliotis D, Alaswad K et al (2018) Prevalence, presentation and treatment of ‘balloon undilatable’ chronic total occlusions: insights from a multicenter US registry. Catheter Cardiovasc Interv 91(4):657–666. https://doi.org/10.1002/ccd.27510
35. Brilakis ES, Banerjee S (2011) Crossing the “balloon uncrossable” chronic total occlusion: Tornus to the rescue. Catheter Cardiovasc Interv 78(3):363–365. https://doi.org/10.1002/ccd.23319
36. Vo MN, Christopoulos G, Karmpaliotis D et al (2016) Balloon-assisted microdissection “BAM” technique for balloon-uncrossable chronic total occlusions. J Invasive Cardiol 28(4):E37–E41
37. Tsutsui RS, Sammour Y, Kalra A et al (2021) Excimer laser atherectomy in percutaneous coronary intervention: a contemporary review. Cardiovasc Revascularization Med 25:75–85. https://doi.org/10.1016/j.carrev.2020.10.016
38. Abdelaziz A, Elsayed H, Hamdaalah A et al (2024) Safety and feasibility of rotational atherectomy (RA) versus conventional stenting in patients with chronic total occlusion (CTO) lesions: a systematic review and meta-analysis. BMC Cardiovasc Disord 24(1):4. https://doi.org/10.1186/s12872-023-03673-2
39. Ye YC, Zhao XL, Du JJ et al (2020) Efficacy and safety of balloon-assisted microdissection with Sapphire® II 1.0-mm balloon in balloon-uncrossable chronic total occlusion lesions. J Int Med Res 48(10):300060520965822. https://doi.org/10.1177/0300060520965822
40. Rawlins J, Din JN, Talwar S et al (2016) Coronary intervention with the excimer laser: review of the technology and outcome data. Interv Cardiol 11(1):27–32. https://doi.org/10.15420/icr.2016:2:2
41. Tomey MI, Kini AS, Sharma SK (2014) Current status of rotational atherectomy. JACC Cardiovasc Interv 7(4):345–353. https://doi.org/10.1016/j.jcin.2013.12.196
42. Lyu JJ, Liu Y, Gurm HS et al (2023) Electroplating a miniature diamond wheel for grinding of the calcified plaque inside arteries. Med Eng Phys 113:103969. https://doi.org/10.1016/j.medengphy.2023.103969
43. Sakes A, Lageweg M, van Starkenburg RIB et al (2022) Crossing total occlusions using a hydraulic pressure wave: development of the *Wave* catheter. Front Med Technol 4:851927. https://doi.org/10.3389/fmedt.2022.851927
44. Duer MJ, Friscić T, Proudfoot D et al (2008) Mineral surface in calcified plaque is like that of bone: further evidence for regulated mineralization. Arterioscler Thromb Vasc Biol 28(11):2030–2034. https://doi.org/10.1161/ATVBAHA.108.172387
45. Riel LP, Dion S, Brouillette M et al (2014) Characterization of

calcified plaques retrieved from occluded arteries and comparison with potential artificial analogues. In: Proceedings of the ASME International Mechanical Engineering Congress and Exposition, Article V003T03A018.
https://doi.org/10.1115/imece2014-38152

46. Zheng YH, Lyu JX, Liu Y et al (2018) Grinding wheel motion and force during plaque removal by rotational atherectomy in angulated coronary artery. In: Proceedings of the ASME 13th International Manufacturing Science and Engineering Conference, Article V001T05A010.
https://doi.org/10.1115/msec2018-6686
47. Li XX, Yang JQ, Chernjavsky P et al (2023) Experimental investigation of the calcified plaque material removal rate in coronary rotational atherectomy. J Med Devices 17(4):041001.
https://doi.org/10.1115/1.4063671
48. Liu Y, Liu Y, Zheng YH et al (2019) Catheter thermal energy generation and temperature in rotational atherectomy. Med Eng Phys 70:29–38.
https://doi.org/10.1016/j.medengphy.2019.06.014
49. Shih AJ, Liu Y, Zheng YH (2016) Grinding wheel motion, force, temperature, and material removal in rotational atherectomy of calcified plaque. CIRP Ann 65(1):345–348.
https://doi.org/10.1016/j.cirp.2016.04.012
50. Zhu ZJ, Gao CH, Huang ZR et al (2022) Evolution of novel grinding tool in removing coronary artery calcification tissue process. Med Eng Phys 109:103893.
https://doi.org/10.1016/j.medengphy.2022.103893
51. Gao CH, Zhu ZJ, Huang ZR et al (2023) Performance of novel 3D printing tools in removing coronary-artery calcification tissue. Bio-Des Manuf 6(4):390–404.
https://doi.org/10.1007/s42242-022-00228-w
52. Zheng YH, Liu Y, Liu Y et al (2016) Experimental investigation of the grinding force in rotational atherectomy. Proc Manuf 5:838–848.
https://doi.org/10.1016/j.promfg.2016.08.069
53. Zheng YH, Belmont B, Shih AJ (2016) Experimental investigation of the abrasive crown dynamics in orbital atherectomy. Med Eng Phys 38(7):639–647.
https://doi.org/10.1016/j.medengphy.2016.04.006
54. Zheng YH, Liu Y, Pitre JJ et al (2018) Computational fluid dynamics modeling of the burr orbital motion in rotational atherectomy with particle image velocimetry validation. Ann Biomed Eng 46(4): 567–578.
https://doi.org/10.1007/s10439-018-1984-z
55. Sharma SK, Tomey MI, Teirstein PS et al (2019) North American expert review of rotational atherectomy. Circ Cardiovasc Interv 12(5):e007448.
https://doi.org/10.1161/CIRCINTERVENTIONS.118.007448
56. Liu Y, Li BZ, Zheng YH et al (2017) Experiment and smooth particle hydrodynamics simulation of debris size in grinding of calcified plaque in atherectomy. CIRP Ann 66(1):325–328.
https://doi.org/10.1016/j.cirp.2017.04.090
57. Zheng YH, Liu Y, Liu Y et al (2019) Multigrain smoothed particle hydrodynamics and Hertzian contact modeling of the grinding force in atherectomy. J Manuf Sci Eng 141(4):041015.
https://doi.org/10.1115/1.4042603